



MoO₃ Nanoclusters Decorated on TiO₂ Nanorods for Oxidative dehydrogenation of ethane to ethylene

Bipul Sarkar^{a,b}, Reena Goyal^a, L.N. Sivakumar Konathala^a, Chandrashekar Pendem^a, Takehiko Sasaki^c, Rajaram Bal^{a,*}

^a Nano Catalysis Area, Catalytic Conversion & Processes Division, CSIR-Indian Institute of Petroleum, Dehradun 248005, India

^b Synthetic & Applied Chemistry Area, Chemical Sciences Division, CSIR-Indian Institute of Petroleum, Dehradun 248005, India

^c Department of Complexity Science and Engineering, Graduate School of Frontier Sciences, The University of Tokyo, Kashiwanoha, Kashiwa-shi, Chiba 277-8561, Japan

ARTICLE INFO

Article history:

Received 6 December 2016

Received in revised form 12 June 2017

Accepted 13 June 2017

Available online 15 June 2017

Keywords:

Ultrathin TiO₂

MoO₃ nanoclusters

Oxidative dehydrogenation

Ethane

Ethylene

ABSTRACT

Preparation of metal oxide supported nanostructure appears to be interesting and challenging because of the well-defined morphology and highly accessible active sites responsible for catalysis. Here we present an easy approach to synthesize a novel hybrid material composed of highly dispersed MoO₃ nanoclusters on TiO₂ nanorods of diameter 80–150 nm and length between 1–1.5 μm. These hybrid nanostructure catalysts exhibited excellent oxidative dehydrogenation activity for the conversion of ethane to ethylene with an ethylene yield of 50.7% in the presence of O₂. The result shows markedly high synergy between the surface Mo⁺⁶ and ultrathin TiO₂ nanorods, which selectively activates the C–H bond of ethane for the production of ethylene.

© 2017 Elsevier B.V. All rights reserved.

1. Introduction

The demand for light olefins, serve as feedstock for the synthesis of a wide variety of chemicals, is increasing contentiously. Ethylene is one of the main building blocks in the petrochemical industry and used as a feedstock for numerous processes like the production of ethylene oxide, ethylbenzene, a precursor to ethylene glycol and styrene, etc. Global annual ethylene production is increasing gradually in ethylene production over the last 25 years and over 143 million tons per annum (mtpy) of ethylene are produced and used in 2013, worldwide [1,2]. Based on the abundant accessibility of the light hydrocarbon; ethane is mainly derived from natural gas or naphtha cracking. Naphtha cracking in the presence of steam remains the major source of ethylene globally [3,4], but the high endothermicity of this process consumes a lot of energy and produces a heavy amount of coke. The industrial method for the production of ethylene is referred to steam cracking, which is a very energy intensive process and required extremely high temperature (>800 °C). Also, the process produced CO₂ (1.5–3 tons of CO₂ per ton of ethylene produced) [4–6], a greenhouse gas is the main disadvantage of this process. Moreover, the restrictions for CO_x,

NO_x emission will drive the investors toward energy-efficient and environmentally friendly production of ethylene in the near future. Compared to the conventional steam cracking method of dehydrogenating alkanes to olefins and current catalytic dehydrogenation processes, oxidative dehydrogenation (ODH) could reduce costs, lower greenhouse-gas emissions, and save energy [5–7]. Therefore, oxidative dehydrogenation (ODH) of ethane can be considered as environmentally benign in contrast to the other available processes. The associated capital and operational cost can be reduced by eliminating the need for a furnace and decoking shutdowns, lowering operating temperatures, reducing material demands and using a greater proportion of the alkanes in the olefin conversion process. Besides, only 48–50% yield can be obtained in the existing steam cracker [8], and for ODH process, a maximum yield of 45–60% can be achieved [9]. In this context, oxidative dehydrogenation of ethane has grown much interest as the potential alternative to produce high ethylene yield compare to any other processes. Considerable effort has been made on ODH of ethane with Ni, Mo and W based catalyst over group 5 metals [10–17]. These results also suggest that the catalyst support can affect ODH performance.

Materials with controlled size, shape, composition and internal structural assemblies from different synthetic strategies have been extensively studied [18], because it allows the properties of nanocrystals to be tailored, thus enhancing their application for nano-reactors, drug delivery, gas sensors, catalyst, energy stor-

* Corresponding author.

E-mail addresses: raja@iip.res.in, rajab.73@yahoo.com (R. Bal).

age, photons adsorbent materials and biomedical research [19–23]. Shape-controlled TiO₂ nanomaterials have attracted considerable research interest because of their enormous potential application as catalytic support materials, photocatalyst, and solar cell application, intercalated electrodes for Li-ion batteries and as super capacitors [24–28]. Although, over the past decade, a large number of synthesis methods have been applied to fabricate TiO₂ nanostructures; including sol-gel method, template-assisted method, seed growth method and hydrothermal processes [29–32], but the preparation of TiO₂ nanostructure with controlled shape and size are still a challenge for the researchers. There are several reports of the preparation of nanostructured TiO₂, (a comparison can be found in Table S1; in supporting information) but most of the preparation methods involve the use of hazardous inorganic acids such as HF, HCl etc. and the question of reproducibility not been claimed in most of the cases [33,34]. In contrary, support materials in nanometer range have presented improved physical and chemical properties compare to their bulk counterpart [35] and have been proven to be beneficial, especially in catalysis [36–38]. Therefore, the precise modification of surfaces of those supported nanomaterials by changing the shape and size could facilitate the control tuning of the catalytic properties [39]. Nanoclusters (of <1 nm) have approximately 50% atom located on the external surface and have their valence and co-ordination sphere not fully saturated, and hence they show very high activity in catalysis [40]. The preparation of nanoclusters supported on nanocrystalline metal oxide remains a challenge for the catalysis researchers [41,42]. We report a simple preparation of highly dispersed MoO₃ nanoclusters supported on TiO₂ nanorods. The preparation method is very simple and large quantity (up to 20 g) material can be obtained in a single batch.

In this work, we demonstrate a simple method for the preparation of highly dispersed MoO₃ nanoclusters supported on TiO₂ nanorods, and it was found that the material is highly active for the oxidative dehydrogenation of ethane to ethylene in a continuous process at atmospheric pressure. An ethane conversion of 55.2% with ethylene selectivity of 92.1% can be achieved without any severe deactivation up to 80 h over the catalyst.

2. Experimental section

2.1. Materials synthesis

A typical preparation of ultrathin TiO₂ nanorods are as follows: 5 ml titanium isopropoxide were taken in 75 ml ethanol, and 0.2 g octadecyldimethyl (3-trimethoxy silylpropyl) ammonium chloride was added drop wise under vigorous stirring [43,44]. The pH of the mixed solution was adjusted to 7–10 by the addition of 1(M) NaOH solution. Finally, the mixing gel was heated at 80 °C for 1–2 h. The resultant mixture was transferred to a Teflon-lined stainless steel autoclave at 180 °C for 24 h. The white precipitate (TiO₂) was collected by filtration, washed thoroughly with distilled water, ethanol and dried at 100 °C overnight. Finally, the dried TiO₂ material was subjected to calcination at 700 °C with a temperature ramp of 1.5 °C/min in air for 4 h. After successful calcination 0.9–1.1 g, TiO₂ nanorod was obtained per batch.

Supported Mo catalyst was prepared by the following method; 0.2108 g (1.04 mmol) MoCl₃ was mixed with 30 ml ethanol under continuous stirring. 1.04 mmol PVP-40 (Polyvinylpyrrolidone-40) were added dropwise, and the solution was kept at 60 °C for 30 min. Then, 2 g prepared TiO₂ was suspended with 20 ml ethanol with continuous stirring for 1 h and mixed with the Mo-PVP mixture very slowly and stirred for another 2 h at 60 °C. The mixture was dried overnight at 80 °C and calcined at 700 °C for 4 h in the air. The prepared catalysts were denoted as (Mo wt%)Mo/TiO₂. For comparison purpose, we also prepared Mo catalyst using commercial

TiO₂ (~21 nm particle size) nano-powder and the catalyst were denoted as 5%Mo-TiO₂^{NP}. The catalyst was also prepared by physical mixing with commercial TiO₂ and commercial MoO₃ (5% wt. respect to TiO₂) and denoted as 5%Mo-TiO₂^{PM}. The catalyst prepared by co-precipitation method by taking titanium isopropoxide, and MoCl₃ is denoted as 5%Mo-TiO₂^{CP}. The catalyst prepared by conventional impregnation method by taking MoCl₃ using prepared TiO₂ nanorods and denoted as 5%Mo-TiO₂^{Imp}.

2.2. Oxidative dehydrogenation of ethane

The oxidative dehydrogenation of ethane to ethylene was carried out in a fixed-bed down flow quartz reactor at atmospheric pressure. Typically 200 mg palletized granular catalyst (followed by sieved, 0.180 mm) diluted with 5% porcelain beads was placed in between two quartz wool plugged in the center of the 6 mm quartz reactor. ODH of ethane was carried out in the temperature range between 350 to 650 °C. The gas hourly space velocity (GHSV) was varied between 10000 ml g⁻¹h⁻¹ to 30000 ml g⁻¹h⁻¹ with a molar ratio of C₂H₆:O₂: He of 1:1:8. The reaction products were analyzed using an online gas chromatography (Agilent 7890A) equipped with a flame ionization detector using Al₂O₃/KCl capillary column (for analyzing C₁–C₄ gases) and thermal conductivity detector using PoraPak-Q (for analyzing O₂ and CO₂) and molecular sieve (for analyzing H₂). The conversion and selectivity of the catalyst were calculated as:

$$\text{Conversion (mole\%)} = \frac{\text{Moles of ethane reacted (mole\%)}}{\text{Moles of ethane initially used (mole\%)}} \times 100$$

$$\text{Selectivity (mole\%)} = \frac{\text{Moles of products (mole\%)}}{\text{Moles of ethane reacted (mole\%)}} \times 100$$

2.3. Materials characterization

The microstructures of the catalyst surfaces of the samples were observed using scanning electron microscopy–energy dispersive X-ray spectroscopy (SEM-EDS) (FEI Quanta 200F), field emission scanning electron microscopy (FE-SEM) (FEI Quanta 200F), and transmission electron microscopy (TEM) (JEM-2010DM, JEOL). The crystal structure was confirmed by powder X-ray diffraction (XRD) (Bruker D8 Advance, Bruker Corp.) using Cu K α (λ = 0.154 nm) as an incident beam. The BET surface area of the catalysts was examined by N₂ adsorption-desorption isotherms at –196 °C (Belsorbmax, BEL, Japan) using BET equation. Pore size distributions were determined using Barrett-Joyner-Halenda (BJH) model of cylindrical pore approximation. Raman spectrum of the sample was measured using a micro-Raman spectroscopy (XploRA, HORIBA, Ltd.). The incident light used for the experiments was a 532 nm semiconductor laser. The chemical state of the samples was carried out by X-ray photoelectron spectroscopy (XPS) (K-Alpha, Thermo Scientific Corp.). The monochromatized X-ray Mg K α radiation (1253.6 eV) was used. The core levels were calibrated by reference to the first component of the C 1s core level peak (unfunctionalized hydrocarbons) set at 284.6 eV. Extended X-ray absorption fine structure spectroscopy (XAFS) measurements of Cu-K edge were carried out at the High Energy Accelerator Research Organization (KEK-IMMS-PF), Tsukuba, Japan. The EXAFS spectrum of the fresh catalyst was measured in the transition mode, whereas for the spent catalyst the EXAFS spectrum was measured in the fluorescence mode using a Lytle detector with Ar gas and spectra were taken at BL-7C and BL-9C at the Photon Factory, Tsukuba, Japan. The electron storage ring was operated at 2.5 GeV and 450 mA; synchrotron radiation from the storage ring was monochromatized by a Si(111) channel-cut crystal. Ionized chamber, which was used as detectors for incident X-ray (I₀) and transmitted X-

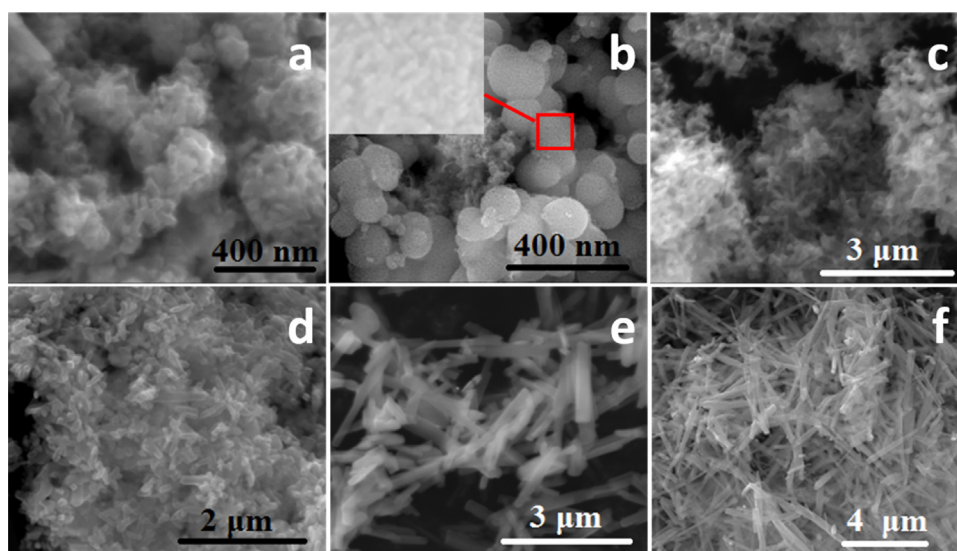


Fig. 1. SEM images of TiO₂ nanoarchitecture at (a–f) 3, 6, 9, 12, 18 and 24 h, at pH 7, Other preparative parameters are [organosilane] = 0.2 g, [Ti[OCH(CH₃)₂]₄] = 5 ml, and 75 ml [ethanol].

Table 1
Physio-chemical properties of the catalyst.

Catalyst	BET Surface area (m ² /g)	Mo dispersion ^a	surface density Mo (atom/nm ²)	H ₂ calculated (mmol/g)	H ₂ consumed ^b (mmol/g)
TiO ₂	52.6	–	–	–	–
2.5%Mo–TiO ₂	45.3	52.3	4.3	1.563	1.443
5%Mo–TiO ₂	42.1	50.9	6.8	3.126	2.886
5%Mo–TiO ₂ ^{NP}	26.5	12.0	3.2	3.126	2.886
5%Mo–TiO ₂ ^{PM}	19.4	9.4	1.9–2.9	3.126	2.886
5%Mo–TiO ₂ ^{CP}	16.9	11.7	2.9	3.126	2.886
5%Mo–TiO ₂ ^{Imp}	38.5	15.9	3.1	3.126	2.886
10%Mo–TiO ₂	37.9	39.3	3.9	6.253	5.771
15%Mo–TiO ₂	29.6	33.1	2.9	9.379	8.657

^a H₂ chemisorption on Micromeritics, Auto Chem II 2920; detailed in supporting information.

^b Calculated from TPR.

ray (I), were filled with N₂ mixture gas, respectively. The angle of the monochromators was calibrated with Mo foil. The EXAFS raw data was analyzed with UWXAFS analysis package [45] including background subtraction program AUTOBK [46] and curve fitting program FEFFIT [47]. The amplitude reducing factor, S_{00}^2 was fixed at 1.0. The backscattering amplitude and phase shift were calculated theoretically by FEFF 8.4 code [48]. ATOMS [49] were used to obtain FEFF input code for crystalline materials. The angle of the monochromators was calibrated with Mo foil.

Temperature programmed reduction (TPR) and H₂ chemisorption experiments were carried out in a Micromeritics, Auto Chem II 2920 instrument connected with a thermal conductivity detector (TCD). Before TPR, the catalysts were also heated at 650 °C for 2 h in helium and then placed in 10% H₂/Ar with a flow rate of 40 ml min^{−1} in the temperature range of 40–1000 °C with an increment of 10 °C/min. UV–vis spectra were recorded at room temperature without exposing the sample to air using Shimadzu UV–vis Spectrophotometer (Serial No. A11665101641; Model: UV-2600 230 V, with a diffuse reflectance accessory, in the 200–800 nm wavelength range). UV Probe 2.43 software was used for analysis. Anhydrous BaSO₄ was used as a reference. The Kubelka Munk function $F(R)$ was plotted against the wavelength (in nm). Thermogravimetric analysis (TGA) patterns were recorded on a Perkin-Elmer Diamond TGA apparatus under N₂ atmosphere and a heating rate of 10 °C/min. Inductively Coupled Plasma Atomic Emission Spectrometer has been collected on a Leeman Labs, Inc, (USA) PS 3000 UV apparatus. The amount of coke deposited on the catalyst has been calculated from ICP analysis.

3. Result and discussion

3.1. Formation mechanism of free-standing ultrathin TiO₂ nanorods

The SEM images of the different Mo–TiO₂ materials are shown in Figs. 1 and 2. The representative TEM images of the 5%Mo–TiO₂ samples are shown in Fig. 3. Fig. 3D clearly displays that the inter planner distance between two neighboring fringes is 0.35 nm, which corresponds to (101) plane of anatase TiO₂. The (101) lattice plane has the low surface free energy, and it can be formed easily. XRD analysis also exhibited (Fig. 7a) the highest intensity peak at a 2θ value of 25.3, which corresponds to the (101) plane (JCPDS card no. 84-1286). Although there are several reports of the preparation of TiO₂ nanostructure by the hydrothermal method; the exact mechanism behind the formation of TiO₂ nanostructure are not clear. To investigate the mechanism for the formation of TiO₂ nanorods, SEM images were taken at a different stage during the crystallization process. The possible formation mechanism is shown in Scheme 1. The formation mechanism of such a nanostructure based on semiconductor materials in solutions follows the basic crystal growth mechanism: Ostwald ripening and oriented attachment [50]. Most of the researchers believed that TiO₂ nanostructure formation occurs by dissolution re-precipitation of self-assembled micelles in the presence of surfactant. Based on our investigation, we believe that formation of free-standing ultrathin TiO₂ is the combination of Ostwald ripening [51] and self-assembly processes for oriented attachment. Initially, the hydrolysis of tita-

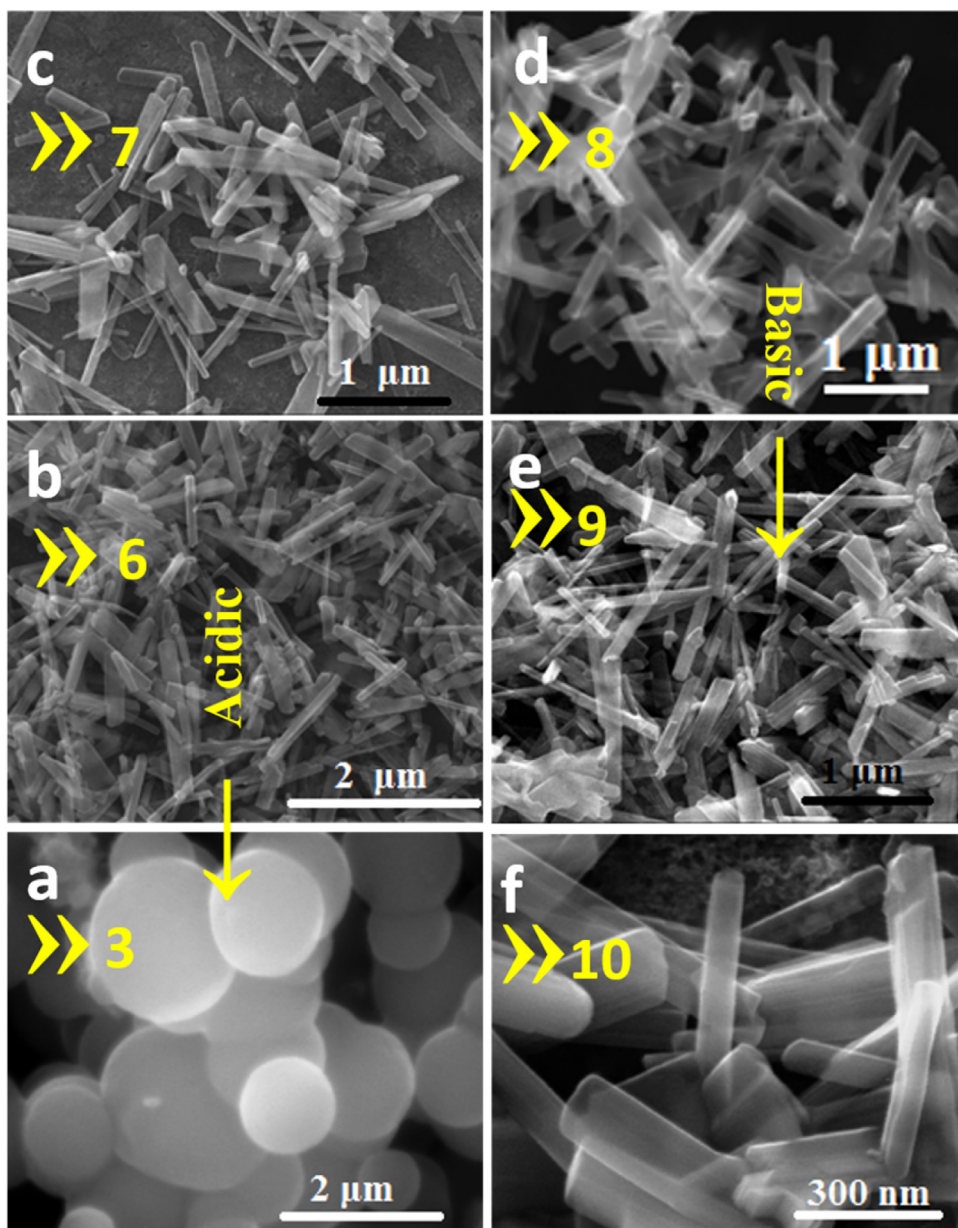


Fig. 2. SEM micrographs at different pH; pH of all the material is denoted by the double arrow, showing the reproducibility of the proposed synthesis method detailed above.

nium isopropoxide takes place in an ethanol medium similar to that reported by Hosono et al. [52] and more recently by Wang et al. [53] in an aqueous medium for the growth of 2D TiO_2 nanostructures. As a result, numerous tiny titanium hydroxide nuclei appeared in the presence of octadecyldimethyl (3- trimethoxy silylpropoxy) ammonium chloride [ODS]. The growth depends on the pH of the solution. As template octadecyldimethyl (3- trimethoxy silylpropoxy) ammonium chloride was involved, initially the freshly tiny titanium hydroxide nuclei grow and aggregate to minimize their surface area through Ostwald ripening. To further investigate the formation mechanism sample were collected at different stages of the crystallization process and was analyzed by SEM in low vacuum mode. Fig. 1 shows that aggregated tiny assembly of titanium hydroxide has started to grow after 3 h of hydrothermal treatment and take 18 h to start the nanorod formation (Fig. 1e).

Surfactant octadecyldimethyl (3- trimethoxy silylpropoxy) ammonium chloride will form an ionic head in the solution, and a co-operative self-assembly between tiny titanium hydroxide nuclei

and ionic part of the template octadecyldimethyl (3- trimethoxy silylpropoxy) ammonium chloride exists. The template then starts to adsorb titanium hydroxide aggregates (which has been strongly assisted by pH) and form distorted small crystallites. The different TiO_2 nanostructures, which can be formed depending on the pH of the solution (Fig. 2). It is a well-established phenomenon that the curvature of an ionic micelle can be turned from spherical to rod-like micelle by adding a certain additive [54]. In this preparation method, spherical Ti micelles (after 3 h, Fig. 1a) were transferred into rod-shaped micelles (after 18 h, Fig. 1e); as a result attractive electrostatic interaction between octadecyldimethyl (3- trimethoxy silylpropoxy) ammonium chloride stabilized negatively titanates ions and positively charged sodium ions, where Na^+ ion enhance the symmetry breaking anisotropic growth through selective adsorption onto (101) plane of TiO_2 . Thus the decrease in surface free energy of TiO_2 seed crystal in particular direction (101) results in the formation of 1-D rod-like structure, which acts as the nucleating agent for the growth of different TiO_2 nanorods.

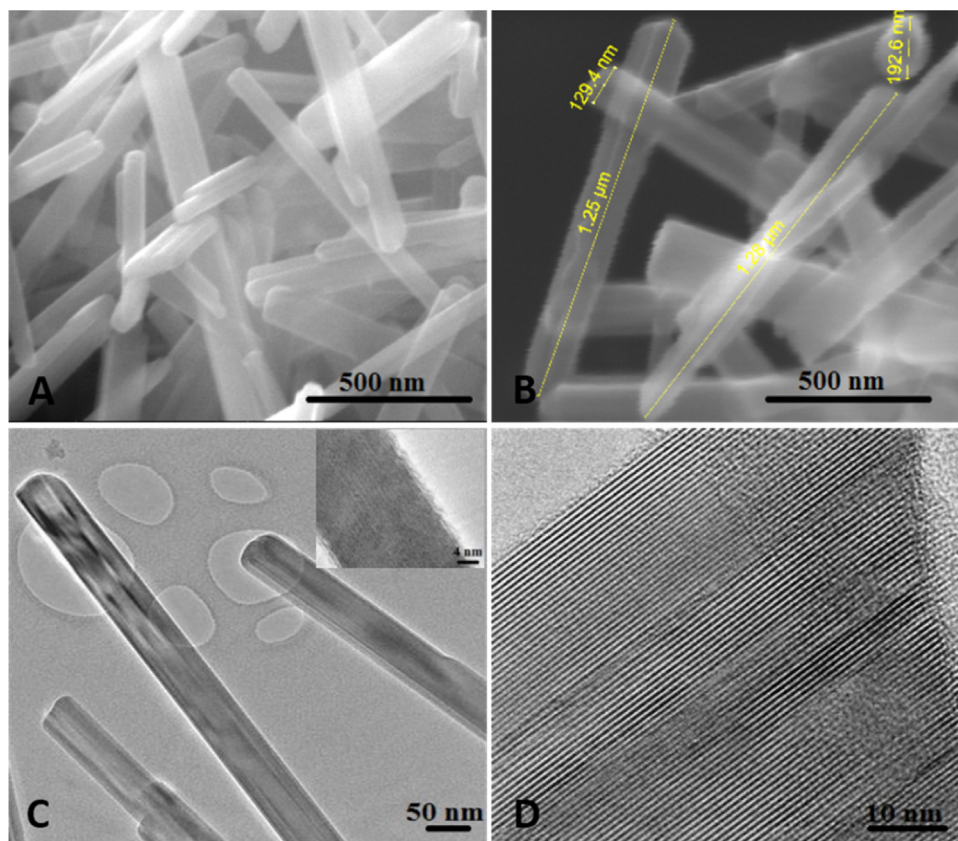
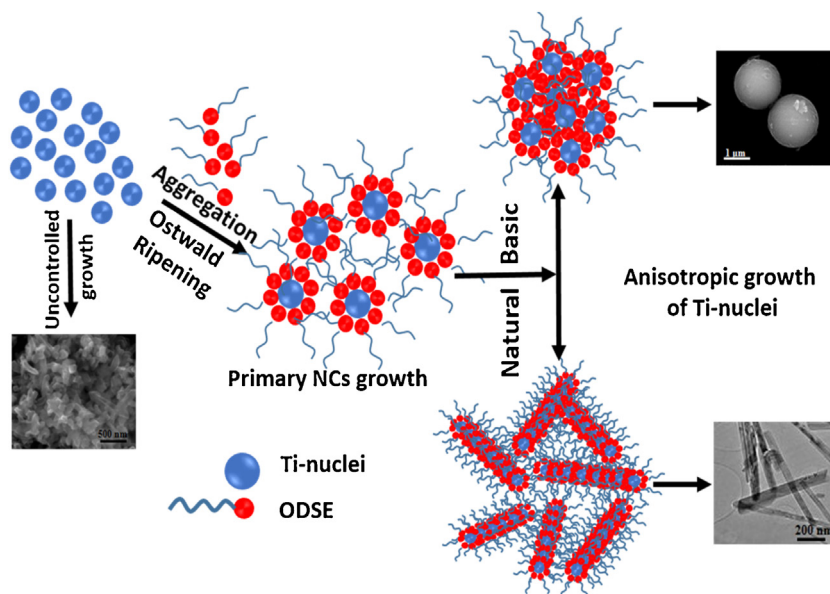


Fig. 3. Electron microscopy images of Pure TiO_2 and Mo-TiO_2 : (A, B) SEM images of pure TiO_2 and 5% Mo-TiO_2 respectively; (C, D) TEM images at a low and high magnification of 5% Mo-TiO_2 catalyst, respectively.



Scheme 1. Schematic of the shape-controlled synthesis of nanorods. ODSE = octadecyldimethyl (3- trimethoxy silylpropoxy) ammonium chloride.

The morphology of the different TiO_2 materials at different pH are shown in Fig. 2. It was observed that in an acidic medium (very low concentration of Na^+ ion) morphology looked like spherical (Fig. 2a), whereas at higher pH (higher concentration of Na^+ ion) formation of rod-like morphology occurs (Fig. 2b–f).

3.2. Morphology of Mo-TiO_2 materials

The morphology of the prepared TiO_2 was investigated by scanning electron microscopy (SEM) and transmission electron microscopy (TEM). SEM images shows (Fig. 3A) that prepared TiO_2 forms uniformly distributed TiO_2 nanorods of 80–150 nm diameter with a length of 1–1.5 μm . The rod-like morphology remained

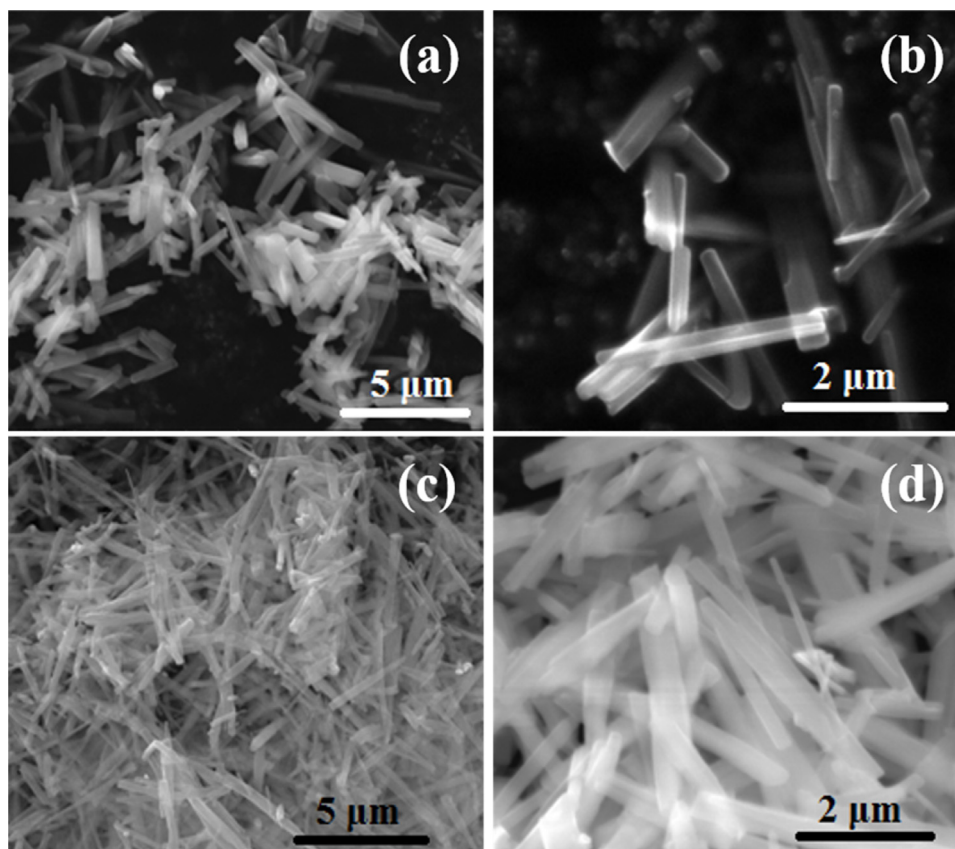


Fig. 4. SEM images of as-prepared TiO_2 (a-b) and Mo-TiO_2 (c-d) respectively.

intact after the loading of MoO_3 as shown in Figs. 3 B and 4. The SEM images of the Mo catalyst prepared for comparison was shown in Fig. S1, in supporting information. TEM images of 5% Mo-TiO_2 catalyst (Fig. 3C and D) show the absence of any Mo species over TiO_2 nanorods, indicating the presence of highly dispersed MoO_x species (as suggested by elemental mapping and EDAX (Figs. S2 and 3, supporting information) and EXAFS analysis; discussed later) over the ultrathin TiO_2 nanorods. Figs. 5 and 6 shows the SEM and TEM micrographs of the 5% Mo-TiO_2 catalysts after 24 h time-on-steam, and it can be visualized that there is no change in morphology of the spent catalyst. The analysis of the surface and bulk composition measured by the ICP (bulk composition) and EDAX (surface composition) analysis for the both fresh and spent catalyst was similar (Fig. 6). The XRD pattern of TiO_2 (Fig. 7a) shows the presence of body center tetragonal anatase phase of TiO_2 ; which was confirmed by the characteristics peaks at 25.3 (101), 37.8 (004), 48.1 (200) and 54.0 (105) peaks as in JCPDS card 84-1286. No peak attributed to any Mo species was observed for 5% Mo-TiO_2 catalyst which also indicates the possible formation of tiny Mo oxide in the form of nanoclusters over anatase TiO_2 nanorods. In contrary, the physically mixed catalyst (5% $\text{Mo-TiO}_2^{\text{PM}}$), MoO_3 (JCPDS card 89-5108) co-exist with Mo_9O_{26} (JCPDS card 89-1466) over anatase TiO_2 . XRD of the reference catalyst also shows similar co-existence of mixed phase (Fig. S4). The specific surface area of the prepared TiO_2 nanowire ($52.6 \text{ m}^2/\text{g}$, Table 1) was found higher than the commercially available titania (Sigma-Aldrich). Although, the surface area was noted to decrease with the loading of Mo from 2.5% to 15%. This might be due to the pore covering caused by the increase in metal loading [55]. While, 5% Mo-TiO_2 catalyst showed a specific surface area of $42.1 \text{ m}^2/\text{g}$ with is higher than the other reference material (Table 1) with the similar loading of Mo. The specific surface area noted for the reference material was found to be 26.5, 19.4,

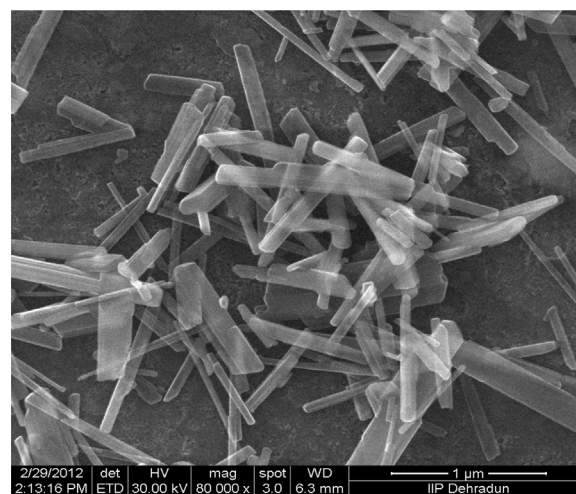


Fig. 5. SEM images of 5% Mo-TiO_2 spent catalyst.

16.9 and $38.5 \text{ m}^2/\text{g}$ for 5% $\text{Mo-TiO}_2^{\text{NP}}$, 5% $\text{Mo-TiO}_2^{\text{PM}}$, 5% $\text{Mo-TiO}_2^{\text{CP}}$ and 5% $\text{Mo-TiO}_2^{\text{IMP}}$ respectively. Mo 3d XPS spectra are shown in Fig. 7b. Mo $3d_{5/2}$ binding energy peak appears at 232.6 eV as a singlet along with a satellite peak 235.9 eV confirm the presence of Mo^{6+} for 5%- TiO_2 catalyst [56]. This observation is in good agreement with the XRD and Raman (discussed later) analysis. For the spent catalyst the Mo $3d_{5/2}$ peak shifted to 229.6 eV confirming the reduction of Mo^{6+} to Mo^{4+} . XPS analysis also shows that the support Ti 2p (Fig. 7d) also appeared as a singlet at 485.5 eV due to the presence of pure TiO_2 . H_2 -TPR analysis was carried out to check the reducible behavior nature of the catalyst. As TiO_2 has a very high and negative, free energy of formation, so it is very hard to

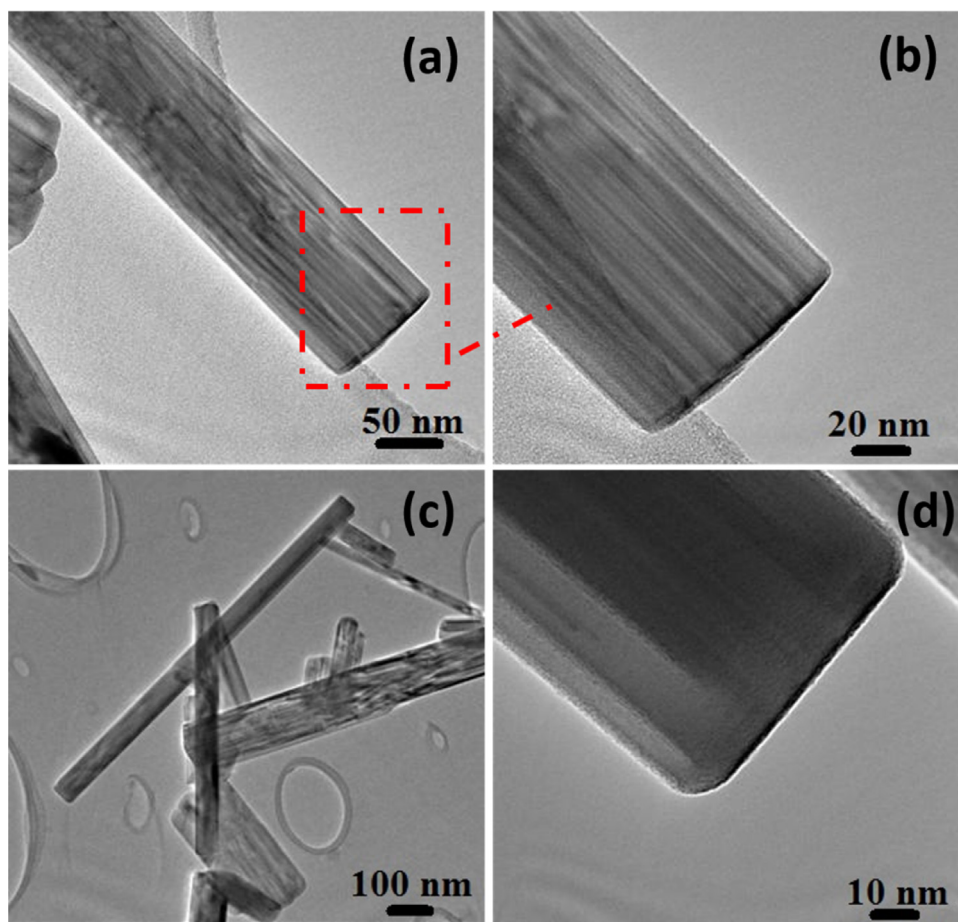


Fig. 6. TEM images of the spent 5%Mo-TiO₂ catalyst.

reduce (in Fig. 8 below 1000 °C [57]. H₂ TPR of 5%Mo-TiO₂ shows several hydrogen consumption peaks between 500 to 1000 °C for the reduction of different Mo species. Deconvolution shows four individual peaks at 568, 684, 784 and 920 °C. These peaks can be attributed the stepwise reduction of Mo⁶⁺ species to metallic Mo [58,59].



The peak at 568 °C can be attributed to the reduction of Mo⁺⁶ to Mo⁺⁴ and the broad peaks between 650 and 800 °C which are the combination of two peaks appear to be the reduction of Mo⁺⁶ to Mo^{δ++} (those Mo^{δ+} and Mo^{δ++} can be assumed as Mo⁺³ and Mo⁺² oxidation state of molybdenum). The peak at 920 °C is the reduction of Mo^{δ++} to metallic Mo (Mo⁰).

It was believed that anatase phase transforms to rutile phase between 550 to 650 °C during calcination, but we did not observe any phase transformation (Fig. S5a, in supporting information). It has to be noted that, the organosilane template which was used during the preparation of TiO₂ was not removed properly. The amount of silica present was so small that it was not detected by energy dispersive analysis by x-ray (EDAX). This small amount of silica restricts present within the catalyst (as confirmed by XPS, see Fig. S6) the phase transformation during the calcination at 700 °C. Earlier study by Hirano et al. [60] also experienced the same observation and they found that in the case of the TiO₂/SiO₂ composite; the anatase-to-rutile phase transformation was restricted and the anatase-type structure is stable up to 1300 °C with forming any of rutile phase. We have treated the as-prepared TiO₂ nanowire with HF for the complete removal of silica and did the calcination at

two different temperature (at 550 and 700 °C). The result shows that when it was calcined at 550 °C, the sample it was completely anatase while the sample calcined at 700 °C (Fig. S7, in supporting information) it was found that some anatase phase transforms to rutile-type (rutile-anatase mixed) TiO₂. The TGA analysis of the HF treated sample is shown in Fig. S5b, in supporting information; where the exothermic peak at 629 °C was attributed to the latent heat for the phase transformation from metastable anatase TiO₂ to stable rutile phase.

3.3. EXAFS and raman analysis

Detailed structural parameters of the Mo species were obtained by Mo K-edge EXAFS analysis. The curve fitting results are summarized in Table 2. For the shell of the fresh catalyst, the Mo-O bond with a distance of 0.177 nm and coordination no (CN) of 3.39 ± 0.01 were obtained. The small CN indicates the formation of MoO₃ nanoclusters. The clusters were durable under ODH of ethane as confirmed by the EXAFS analysis and Raman spectra of spent catalyst (Figs. 9 and 10). The Mo-O bond length for the spent catalyst was observed at a distance of 0.176 nm with a coordination no of 2.5 ± 0.03 indicates that the Mo species has reduced from MoO₃ to MoO₂ during the catalysis (confirmed by XPS also). The Fourier Transformed Mo K-edge EXAFS spectra for the fresh and spent catalyst is shown in Fig. 9. Fig. 7c shows Raman spectra of the prepared TiO₂ nanorods and 5%Mo-TiO₂ sample calcined at 750 °C. The Raman bands at 144, 197, 398, 514 and 519 (superimposed with 514 cm⁻¹ band), and 639 cm⁻¹ are the characteristic bands for anatase phase of TiO₂ [61]. These typical Raman bands have been attributed to the six Raman active modes of anatase

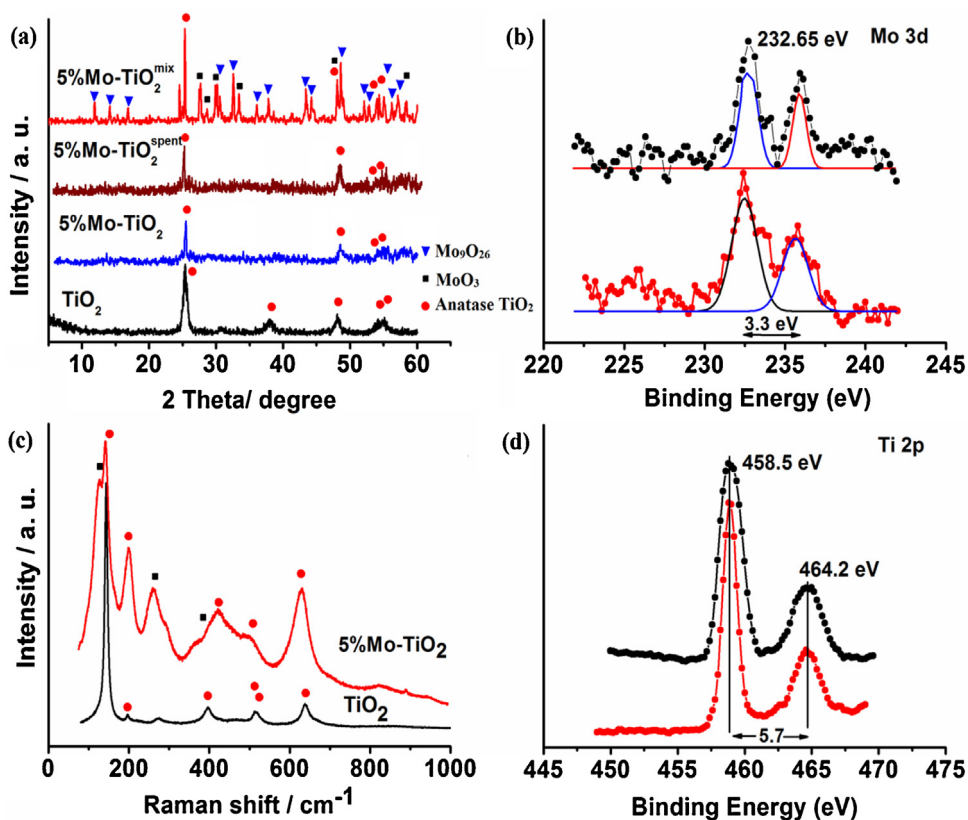


Fig. 7. (a) XRD pattern of pure anatase TiO₂, fresh and spent 5%Mo-TiO₂, and physically mixed 5%Mo-TiO₂. Each peak is labeled as per JCPDS card no 84-1286, 89-5108, and 89-1466. (b) XPS pattern for Mo 3d (fresh in red and spent in black). (c) Raman spectra of pure anatase TiO₂ nanorods, and 5%Mo-TiO₂ catalyst. (d) XPS pattern for Ti 2p (fresh in red and spent in black). (For interpretation of the references to colour in this figure legend, the reader is referred to the web version of this article.)

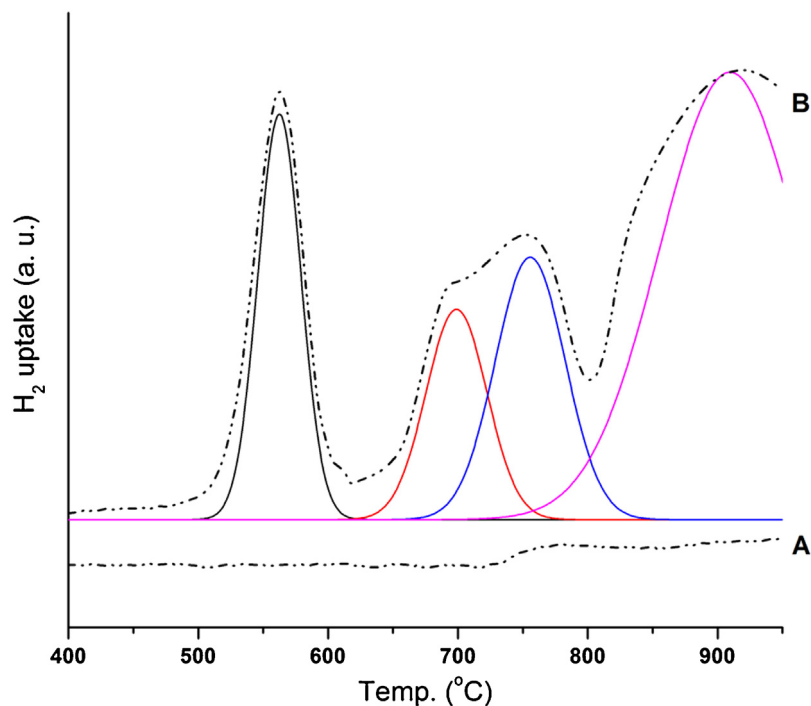


Fig. 8. Temperature Programmed Reduction (TPR) profile of (A) as prepared ultrathin TiO₂ and (B) 5%Mo-TiO₂ (dotted line belongs to original spectra, solid lines belong to deconvoluted spectra).

TiO₂ with the following, Eg, Eg, B1 g, A1 g, B1 g and Eg symmetries respectively [62]. Anatase TiO₂ does not show any Raman bands in the range between 800 and 1100 cm⁻¹. A new band was appeared

at 822 cm⁻¹ for the 5%Mo-TiO₂ catalyst and has been assigned to (monomeric) MoO₃ nanoclusters (not detected by XRD) supported on TiO₂ [63]. The lack of sharp Raman band at about, 822 and

Table 2
Summary of the EXAFS fitting results for Mo catalysts.

	Mo-O				Δk (10 nm ⁻¹)	ΔR (10 nm ⁻¹)	ΔE_0 (eV)	R_f (%)
	R (10 ⁻¹ nm)	CN	DW (nm ²)	Debye temp (K)				
Fresh	1.777 ± 0.023	3.39 ± 0.01	1.639e-3	286.0 ± 6.0	3–14	1.0–2.0	17.6 ± 0.6	0.21
Spent (after 20 h)	1.765 ± 0.028	2.5 ± 0.03	5.980e-4	286.6 ± 8.3	3–14	1.0–2.0	15.7 ± 2.2	2.2

Fitting was achieved with respect to Mo-O path, which is repaired by ATOMS program and MoO₃ crystal structure. The paths of MoO₃ crystal correspond to Mo-O(-Mo). The Mo-O path can be fitted as 0.1765–0.1777 nm that can be attributed to the distance of Mo⁶⁺–O of the dispersed Mo⁶⁺ species. The crystal size of MoO₃ is considered as small since the inclusion of more distant paths does not improve the fittings. CN = coordination number; R = bond length; DW: Debye-Waller factor; Δk : the range of wavenumbers used in the fitting; ΔR : the range of bond distances used in the fitting; ΔE_0 : the shift of the edge-position; R_f : Reliability factor.

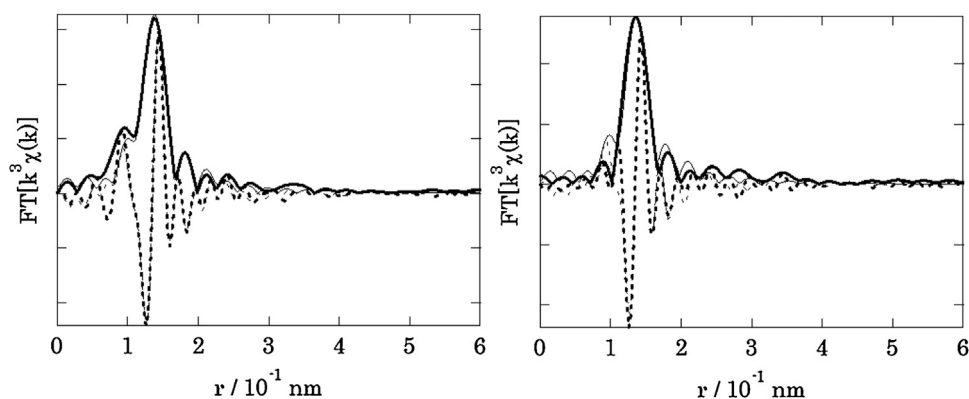


Fig. 9. k^3 -weighted Fourier transform of Mo-K edge EXAFS for the fresh (up) and spent (down) Mo-TiO₂ catalyst.

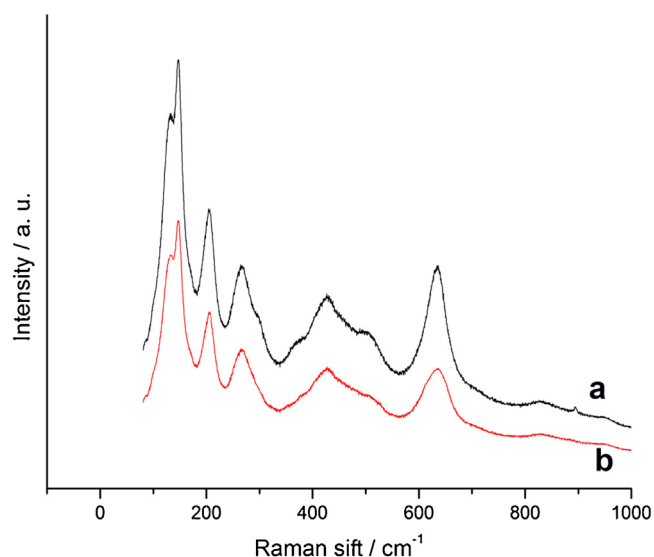


Fig. 10. Raman spectra of (a) fresh and (b) spent 5%Mo-TiO₂ catalyst (after 10 h of reaction).

994 cm⁻¹ indicates the absence of crystalline MoO₃, but amorphous MoO₃ may be present. Additionally, it also demonstrates that the molybdenum oxide species formed easily on the surface of anatase titania [64]. A weak band appeared at ~938 cm⁻¹ were assigned to Mo-O-Mo functionality indicating the presence of polymeric oxomolybdenum species [65].

3.4. In-situ UV and reaction mechanism

The UV-vis spectra were recorded in the diffuse reflectance mode as a function of time, and the spectra of Mo-TiO₂ catalyst are shown in Fig. 11. The spectra were recorded over a pre-treated 5%Mo-TiO₂ catalyst with 10% ethane and oxygen mixture balance

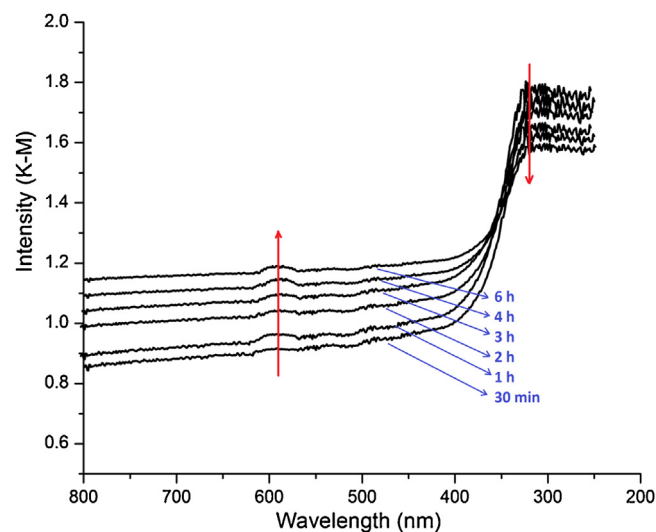
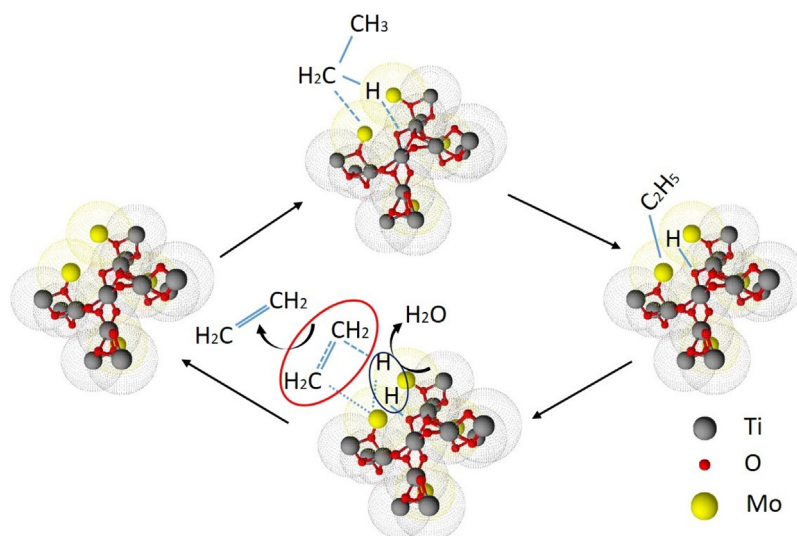


Fig. 11. Diffuse reflectance In-situ UV-vis spectroscopy of Mo-TiO₂ catalyst a function of time under reaction condition.

with He (C₂H₆:O₂: He of 1:1:8) at 550 °C at different reaction time. A general decrease in absorption maxima at around 320 nm was noticed with increasing of reaction time, and a new weak band with absorption maxima at ~590 nm appeared. The presence of an isosbestic point suggests the presence of two different metal species [66], and we assume that one species might be Mo-C₂H₅ species, and the other could be adsorbed [Mo-o]⁺ species.

UV-vis spectra were also taken after pre-treatment of the catalyst with O₂; to see the change of adsorption behavior after oxygen abstraction. It was observed that O₂ pre-treated Mo-TiO₂ catalyst showed similar spectra with the spent catalyst. It has to be noted that O₂ pre-treated spectra show huge absorption in the region of 300–500 nm (in Fig. S8; in supporting information); and the change in absorption maxima for ligand-to-metal charge-transfer bands



Scheme 2. Possible reaction pathways over Mo-TiO₂ catalyst.

Table 3

The performance of the different Mo-TiO₂ catalysts.

Entry	Catalyst	X _c ^c	X _s ^d	Y _{ethylene}	R ^e
1	TiO ₂ nanorods	1.9	62.3	1.1	–
2	TiO ₂ ^{NP}	0.6	24.6	0.1	–
3	MoO ₃ ^{comm}	1.6	27.1	0.4	0.001
4	2.5%Mo-TiO ₂	23.2	92.9	21.5	0.357
5	5%Mo-TiO ₂	55.2	92.1	50.8	0.426
6	5%Mo-TiO ₂ ^{NP}	5.7	59.6	3.4	0.043
7	5%Mo-TiO ₂ ^a	49.2	89.6	44.0	0.379
8	5%Mo-TiO ₂ ^{PM}	5.6	59.1	3.3	0.043
9	5%Mo-TiO ₂ ^b	18.5	64.6	11.9	0.142
10	5%Mo-TiO ₂ ^{CP}	13.2	75.4	9.9	0.051
11	5%Mo-TiO ₂ ^{Imp}	25.7	81.8	21.0	0.100
12	10%Mo-TiO ₂	52.1	87.8	45.7	0.200
13	Mg orthovanadat ^f	5.2	24	–	–
14	Mo–V–Nb mixed oxides ^f	~35	~90	31.0	–
15	Ni–Ta–O mixed oxide ^f	~62	~68	42.1	–
16	Ni–W–O mixed metal oxide ^f	~26	~58	15.0	–

0.2 g catalyst, C₂H₆:O₂: He of 1:1:8, TOS = 4 h, temp. = 550 °C, GHSV = 10000 ml g⁻¹ h⁻¹, all the catalyst been activated at 700 °C with 10% H₂ for 1 h.

^a without activation at 700 °C with 10% H₂ in balance He for 1 h.

^b Mo loaded on HF-etched TiO₂.

^c Conversion and selectivity are in mole%.

^d Selectivity are in mole%.

^e Rate of formation of ethylene in (x 10² mol. gm⁻¹ h⁻¹).

^f data taken from Refs. [8,10,12,16] respectively.

(LMCT) towards higher energy is most possibly due to the oxidation of Mo⁺⁴ to Mo⁺⁶ [67].

The probable catalytic cycle of oxidative dehydrogenation of ethane over Mo-TiO₂ is shown in Scheme 2. We believe, initially, the dissociation of C–H bond of ethane occurs over the distorted body center tetragonal Mo loaded anatase TiO₂ on the Mo^{δ+}–O^{δ-} Lewis pair site [68,69]. Subsequently generated negative alkyl group [–C₂H₅]⁻ adsorb by the Mo ion to form [Mo–C₂H₅] like structure, and the remaining proton [H] binds with the adsorbed oxygen on Mo [70]. Fragmentary stretching of the Mo–O bond increases the Lewis acidity of the Mo atom increases and afterward it polarizes the β-H of the ethyl group (as suggested by Frash et al. with Zn–O) [69]. Then, probably rearrangement occurs to allow ethylene and oxygen to adsorb on [Mo(O)OH]⁺ [71]. This [Mo(O)OH]⁺ cation facilitates to recombine the Brønsted proton attached to the oxygen and release 1 molecule of H₂O [71].

3.5. Catalyst evaluation

The catalytic activity of Mo-TiO₂ catalyst for oxidative dehydrogenation of ethane to ethylene was evaluated at 550 °C under atmospheric pressure. The results are shown in Table 3. It can be clearly visible that Mo-TiO₂ catalysts are catalytically more active compared to pure anatase TiO₂ prepared hydrothermally (entry 1, Table 3). When the reaction was carried out with commercial MoO₃, a negligible ethane conversion of 1.6% with 27.1% ethylene selectivity was noticed, but the catalyst deactivates very rapidly (entry 3, Table 3). The data indicates that MoO₃ are the active species for the reaction. We analyzed the spent MoO₃ catalyzed and found that the agglomeration of the MoO₃ taken place and coke deposition is taking place over the catalyst, which is the main reason for the possible deactivation of the catalyst. Over the 5%Mo-TiO₂ catalyst, an ethane conversion of 55.2% with ethylene formation rate (although ethylene formation rate and selectivity both depend on conversion) of 42.6 mol g⁻¹ h⁻¹ (entry 5, Table 3) was observed.

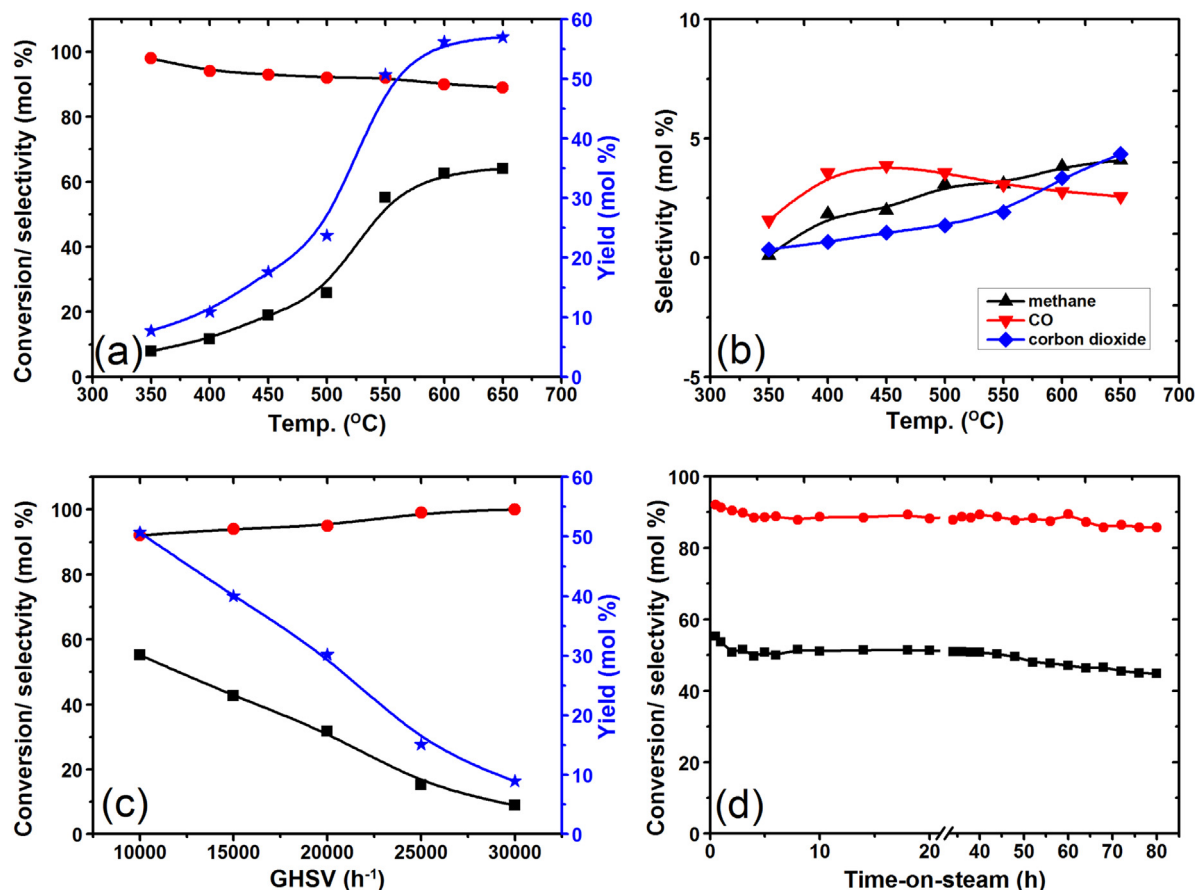


Fig. 12. Effect of (a&b) temperature on the selective oxidative dehydrogenation of ethane to ethylene with 0.2 g catalyst, $C_2H_6:O_2: He$ of 1:1:8, TOS = 1 h, GHSV = 10,000 $ml\ g^{-1}\ h^{-1}$. (c) GHSV as a function of ethane conversion and ethylene selectivity with 0.2 g catalyst, $C_2H_6:O_2: He$ of 1:1:8, TOS = 1 h, temp. = 550 °C. (d) Conversion of ethane and ethylene selectivity over time-on-stream over 5%Mo-TiO₂ catalyst at 550 °C and GHSV = 10,000 $ml\ g^{-1}\ h^{-1}$ for oxidative dehydrogenation. Conversion of ethane [■], Yield [★], selectivity to ethylene [●], CO₂ [◆], methane [▲] and CO [▼].

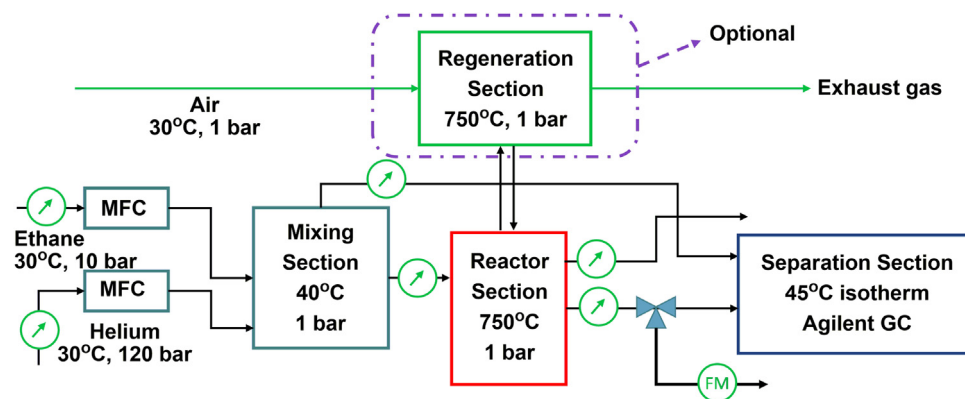


Fig. 13. Preliminary block scheme of oxidative dehydrogenation of ethane.

When Mo loading was decreased to 2.5% (2.5%Mo-TiO₂) the catalyst shows 23.2% ethane conversion keeping the selectivity to ~92.9%. When Mo loading was increased to 10%, the activity decreased (entry 12, Table 3) keeping the selectivity almost same. We believe with higher Mo loading the metal-metal agglomeration leading to larger particle size [72] of 8–15 nm (in Fig. S9, Supporting information) of the molybdenum species (which is the active species) occurs whereas in case of lower loading the availability of active Mo species was less. As a result, the catalyst shows low conversion for the dehydrogenation reaction in the presence of oxygen. This conclusion is in agreement with the obtained metal disper-

sion data and Mo atom density on the TiO₂ nanorods (Table 1), where we found 50.9% Mo dispersion over 5%Mo-TiO₂ catalyst. Experiments were carried out over prepared TiO₂ nanorods (entry 1, Table 3) and TiO₂ nanopowder (entry 2, Table 3) and it was found that the catalyst shows less activity. MoO₃ were loaded over TiO₂ nanopowder using the same preparation method, and the 5%Mo-TiO₂^{NP} catalyst was tested for ODH of ethane. It was found that the catalyst shows 5.7% conversion with ethylene formation rate 4.3 $mol\ g^{-1}\ h^{-1}$ (entry 6, Table 3). MoO₃ supported on commercial TiO₂ (5%Mo-TiO₂^{PM}) also showed less activity and ethylene formation rate. This result indicates that TiO₂ nanorods act as better

support for MoO₃ nanoclusters to show better activity. We also believe that TiO₂ nanorods are not only acting as a support but the interaction between MoO₃ nanoclusters and TiO₂ nanorods playing a crucial role in oxidative dehydrogenation of ethane.

To find out whether isolated TiO₂ nanorods are necessary for the ODH of ethane, much other metal oxide supported was prepared and their catalytic activity was also tested. (entry 1–2, Table S2). The activities of the Mo catalyst supported on the different group IV oxide, such as ZrO₂, HfO₂ were found to be very low. WO₃ particles supported on TiO₂ nanorods were also prepared, and their catalyst activity was also tested (entry 5, Table S2). The catalyst also showed very low activity/selectivity. MoO₃-TiO₂ prepared by impregnation method shows good initial activity but suffers from poor selectivity, and rapid deactivation occurs due to coke deposition 9.3×10^{-5} g_{carbon}/g_{cat}. h. Moreover, we have also noticed that, in the case of 5%Mo-TiO₂^{Imp} catalyst, no decrease in selectivity after 4 h TOS was observed, although conversion goes down with TOS. Thus, it can be concluded that the highly dispersed MoO₃ nanoclusters supported on TiO₂ nanorods are the key parameter for the catalytic activity and low coke deposition of 1.1×10^{-5} g_{carbon}/g_{cat}. h, in which rod-shaped TiO₂ facilitates the formation of ethylene. We also believed that the synergy between highly dispersed MoO₃ nanoclusters and TiO₂ nanorods played a vital role in the formation of ethylene, where support TiO₂ nanorods not only stop coalescence and agglomeration but also favors ethylene formation. The morphology and structure of the spent 5%Mo-TiO₂ catalyst were the same compare to the fresh catalyst (as supported by XRD, SEM, TEM and Raman analysis).

3.6. Effect of reaction parameter

To study the oxidative dehydrogenation of ethane, the effect of parameters such as temperature, GHSV, time-on-stream was also investigated. Steady increase in ethane conversion (Fig. 12a) was observed with the increase in temperature, whereas the rate of increment slows down between 550 °C to 650 °C. Moreover, the selectivity of the major by-product during ODH of ethane was within 1–5% (Fig. 12b) but with the increase in temperature the CH₄ and CO₂ selectivity increases. These results indicate the possible thermal cracking and associated increased rate of complete oxidation of ethane in the presence of excess oxygen on the catalyst surface with elevated temperature. The conversion of ethane decreased from 55.2% to 8.9% with the increase in GHSV from 10000 to 30000 ml g⁻¹ h⁻¹ (Fig. 12b); while the selectivity reaches to 100% at GHSV of 30000 ml g⁻¹.

The activity toward ethane conversion, ethylene selectivity was tested as a function of time-on-stream (TOS) and shown in Fig. 12d. It was observed that the catalyst exhibited a slight decrease from 56.6% to 55.2% in ethane conversion at the initial stage of the reaction but after that, no deactivation was noticed even after 40 h on stream. After 80 h, the catalyst shows 8% deactivation; this data confirmed that 5%Mo-TiO₂ catalyst shows high stability in ODH of ethane to ethylene. Carbon balance calculations were done, and the error was within the acceptable error level of (±5%). For more detailed, a comprehensive process flow scheme (PFS) is presented in Fig. 13.

3.7. Effect of different feed mixtures

Fig. S10, shows the effect of different feed mixtures (C₂H₆:O₂ ratio) on the ODH of ethane. It was found that when the ratio of ethane to oxygen was 0.25, the conversions of ethane and the selectivity to ethylene are 92.0 and 31.5%, respectively. The low selectivity is due to the partial oxidation of ethane with the excess amount of oxygen. When the ratio of ethane to oxygen was 1.0, the conversion of ethane was 55.2%, and the selectivity to ethy-

lene reaches 92.1%. With the further increase of ethane content in the feedstock (a larger C₂H₆:O₂ ratio), both activity of the catalyst decreased to 35.1% whereas the selectivity reaches maxima.

Upon H₂ additions, heat production occurs mainly from the oxidation of H₂ to H₂O with the excess O₂ available to the catalyst surface. Thereby, we co-fed H₂ (C₂H₆:O₂:H₂:He of 1:1:1:7) with the reaction mixture keeping the C₂H₆:O₂ ratio 1. H₂ consumption and H₂O formation (up to 70% of the final value) was observed which indicates to an O₂ conversion of ~100%. As the selectivity topped to 100% of its rules-out the over oxidation due to excess O₂ available to the catalyst surface.

4. Conclusions

In summary, we have explained an easy and reproducible synthesis strategy to prepare highly dispersed MoO₃ supported TiO₂ nanorods using octadecyldimethyl (3-trimethoxy silylpropyl) ammonium chloride as a template. The preparation method is very simple, and it also allows to tune the size and morphology of the TiO₂ nano-architecture by controlling the pH of the synthesis gel. The MoO₃ nanoclusters species supported TiO₂ nanorods can activate the C–H bond of ethane to produce ethylene. The catalyst Exhibits 55.2% ethane conversion and 92.1% ethylene yield at atmospheric pressure and 550 °C; which could be further scale-up in a pilot plant for its practical application.

Acknowledgments

B. S. acknowledges University Grant Commission (UGC), R. G. acknowledges Council for Scientific and Industrial Research (CSIR) India for the fellowship. R. B. thanks, CSIR, New Delhi for financial support in the form of Network Project (CSC-0125 and CSC-0117) under 12 FYP. We also acknowledge Director CSIR-IIP for his support. The authors thank Analytical Science Division, Indian Institute of Petroleum for analytical services.

Appendix A. Supplementary data

Supplementary data associated with this article can be found, in the online version, at <http://dx.doi.org/10.1016/j.apcatb.2017.06.037>.

References

- [1] Y.K. Salkuyeh, T.A. Adams, *Energy Convers. Manage.* 92 (2015) 406–420.
- [2] W.R. True, *Oil Gas J.* 111 (2013) 90–95.
- [3] R. Gudgila, C.A. Leclerc, *Ind. Eng. Chem. Res.* 50 (2011) 8438–8443.
- [4] V.R. Choudhary, S.A. Mulla, *AIChE J.* 43 (1997) 1545–1550.
- [5] S. Wang, K. Murata, T. Hayakawa, S. Hamakawa, K. Suzuki, *Chem. Commun.* (1999) 103–104.
- [6] E. Mamedov, V.C. Corberán, *Appl. Catal. A* 127 (1995) 1–40.
- [7] R. Goyal, B. Sarkar, A. Bag, F. Lefebvre, S. Sameer, C. Pendem, A. Bordoloi, *J. Mater. Chem.* 4 (2016) 18559–18569.
- [8] H.H. Kung, M. Kung, *Appl. Catal. A* 157 (1997) 105–116.
- [9] G. Che-Galicia, R.S. Ruiz-Martínez, F. López-Isunza, C.O. Castillo-Araiza, *Chem. Eng. J.* 280 (2015) 682–694.
- [10] H. Zhu, P. Laveille, D.C. Rosenfeld, M.N. Hedhili, J.-M. Basset, *Catal. Sci. Technol.* 5 (2015) 4164–4173.
- [11] E. Heracleous, A.A. Lemonidou, *J. Catal.* 237 (2006) 175–189.
- [12] H. Zhu, D.C. Rosenfeld, D.H. Anjum, S.S. Sangaru, Y. Saih, S. Ould-Chikh, J.-M. Basset, *J. Catal.* 329 (2015) 291–306.
- [13] H. Zhu, S. Ould-Chikh, D.H. Anjum, M. Sun, G. Biaisque, J.-M. Basset, V. Caps, *J. Catal.* 285 (2012) 292–303.
- [14] H. Zhu, D.C. Rosenfeld, M. Harb, D.H. Anjum, M.N. Hedhili, S. Ould-Chikh, J.-M. Basset, *ACS Catal.* 6 (2016) 2852–2866.
- [15] H. Zhu, D.C. Rosenfeld, D.H. Anjum, V. Caps, J.-M. Basset, *ChemSusChem* 8 (2015) 1254–1263.
- [16] B. Solsona, J.M. López Nieto, P. Concepción, A. Dejoz, F. Ivars, M.I. Vázquez, *J. Catal.* 280 (2011) 28–39.
- [17] H. Zhu, H. Dong, P. Laveille, Y. Saih, V. Caps, J.-M. Basset, *Catal. Today* 228 (2014) 58–64.

- [18] G.R. Patzke, Y. Zhou, R. Kontic, F. Conrad, *Angew. Chem. Int. Ed.* 50 (2011) 826–859.
- [19] Y.G. Lin, Y.K. Hsu, S.Y. Chen, Y.K. Lin, L.C. Chen, K.H. Chen, *Angew. Chem. Int. Ed.* 48 (2009) 7586–7590.
- [20] L. Shi, H. Lin, *Langmuir* 27 (2011) 3977–3981.
- [21] B.K. Teo, X. Sun, *Chem. Rev.* 107 (2007) 1454–1532.
- [22] R. Fan, Y. Wu, D. Li, M. Yue, A. Majumdar, P. Yang, *J. Am. Chem. Soc.* 125 (2003) 5254–5255.
- [23] F. Caruso, R.A. Caruso, H. Möhwald, *Science* 282 (1998) 1111–1114.
- [24] J. Liu, F. Liu, K. Gao, J. Wu, D. Xue, *J. Mater. Chem.* 19 (2009) 6073–6084.
- [25] J. Bitter, K. Seshan, J. Lercher, *J. Catal.* 183 (1999) 336–343.
- [26] S. Chai, G. Zhao, P. Li, Y. Lei, Y.-n. Zhang, D. Li, *J. Phys. Chem. C* 115 (2011) 18261–18269.
- [27] B. O'regan, M. Grätzel, *Nature* 353 (1991) 737–740.
- [28] B.H. Meekins, P.V. Kamat, *ACS Nano* 3 (2009) 3437–3446.
- [29] F. Fabregat-Santiago, H. Randriamahazaka, A. Zaban, J. Garcia-Canadas, G. Garcia-Belmonte, J. Bisquert, *Phys. Chem. Chem. Phys.* 8 (2006) 1827–1833.
- [30] J.H. Jung, H. Kobayashi, K.J. van Bommel, S. Shinkai, T. Shimizu, *Chem. Mater.* 14 (2002) 1445–1447.
- [31] S.-Z. Chu, K. Wada, S. Inoue, S.-i. Todoroki, *Chem. Mater.* 14 (2002) 266–272.
- [32] J. Hulteen, *J. Mater. Chem.* 7 (1997) 1075–1087.
- [33] R. Buonsanti, V. Grillo, E. Carlino, C. Giannini, M.L. Curri, C. Innocenti, C. Sangregorio, K. Achterhold, F.G. Parak, A. Agostiano, *J. Am. Chem. Soc.* 128 (2006) 16953–16970.
- [34] H.G. Yang, C.H. Sun, S.Z. Qiao, J. Zou, G. Liu, S.C. Smith, H.M. Cheng, G.Q. Lu, *Nature* 453 (2008) 638–641.
- [35] S.H. Ahn, W.S. Chi, J.T. Park, J.K. Koh, D.K. Roh, J.H. Kim, *Adv. Mater.* 24 (2012) 519–522.
- [36] B. Sarkar, R.K. Singha, R. Tiwari, S. Ghosh, S.S. Acharyya, C. Pendem, L.S. Konathala, R. Bal, *RSC Adv.* 4 (2014) 5453–5456.
- [37] A.T. Bell, *Science* 299 (2003) 1688–1691.
- [38] R. Schlögl, S.B. Abd Hamid, *Angew. Chem. Int. Ed.* 43 (2004) 1628–1637.
- [39] I. Lee, R. Morales, M.A. Albiter, F. Zaera, *Proc. Natl. Acad. Sci.* 105 (2008) 15241–15246.
- [40] M. Boronat, A. Leyva-Pérez, A. Corma, *Acc. Chem. Res.* 47 (2013) 834–844.
- [41] B. Sarkar, P. Prajapati, R. Tiwari, R. Tiwari, S. Ghosh, S.S. Acharyya, C. Pendem, R.K. Singha, L.S. Konathala, J. Kumar, *Green Chem.* 14 (2012) 2600–2606.
- [42] B. Sarkar, C. Pendem, L.S. Konathala, R. Tiwari, T. Sasaki, R. Bal, *Chem. Commun.* 50 (2014) 9707–9710.
- [43] B. Sarkar, N. Singhal, R. Goyal, A. Bordoloi, L.S. Konathala, U. Kumar, R. Bal, *Catal. Commun.* 74 (2016) 43–48.
- [44] R. Bal, B. Sarkar, R.K. Singha, C. Pendem, S.A. Shankha, S. Ghosh, US20140128653 A1, 2013.
- [45] E. Stern, M. Newville, B. Ravel, Y. Yacoby, D. Haskel, B. Physica, *Condens. Matter* 208 (1995) 117–120.
- [46] M. Newville, P. Livinš, s.Y. Yacoby, J. Rehr, E. Stern, *Phys. Rev. B* 47 (1993) 14126.
- [47] A. Ankudinov, B. Ravel, J. Rehr, S. Conradson, *Phys. Rev. B* 58 (1998) 7565.
- [48] A. Ankudinov, A. Nesvizhskii, J. Rehr, *Phys. Rev. B* 67 (2003) 115120.
- [49] B. Ravel, *J. Synchrotron Radiat.* 8 (2001) 314–316.
- [50] K. Barick, M. Aslam, V.P. Dravid, D. Bahadur, *J. Phys. Chem. C* 112 (2008) 15163–15170.
- [51] J. Mullin, *Crystallization*, 4th edn., Butterworth-Heinemann, Oxford, 2017 (pp. 193).
- [52] E. Hosono, S. Fujihara, K. Kakiuchi, H. Imai, *J. Am. Chem. Soc.* 126 (2004) 7790–7791.
- [53] W. Guo, C. Xu, X. Wang, S. Wang, C. Pan, C. Lin, Z.L. Wang, *J. Am. Chem. Soc.* 134 (2012) 4437–4441.
- [54] R.E. Lamont, W.A. Ducker, *J. Am. Chem. Soc.* 120 (1998) 7602–7607.
- [55] R. Goyal, B. Sarkar, A. Bag, N. Siddiqui, D. Dumbre, N. Lucas, S.K. Bhargava, A. Bordoloi, *J. Catal.* 340 (2016) 248–260.
- [56] C.D. Wagner, G. Muilenberg, *Handbook of X-ray Photoelectron Spectroscopy*, Perkin-Elmer, 1979.
- [57] S. Watanabe, X. Ma, C. Song, *J. Phys. Chem. C* 113 (2009) 14249–14257.
- [58] B. Wang, Y. Yang, L.-J. Li, Y. Chen, *J. Mater. Sci.* 44 (2009) 3285–3295.
- [59] L. Kaluža, D. Gulkova, Z. Vit, M. Zdražil, *Appl. Catal. A* 324 (2007) 30–35.
- [60] M. Hirano, K. Ota, H. Iwata, *Chem. Mater.* 16 (2004) 3725–3732.
- [61] J. Zhang, M. Li, Z. Feng, J. Chen, C. Li, *J. Phys. Chem. B* 110 (2006) 927–935.
- [62] T. Ohsaka, F. Izumi, Y. Fujiki, *J. Raman Spectrosc.* 7 (1978) 321–324.
- [63] G. Tsilomelekis, S. Boghosian, *Phys. Chem. Chem. Phys.* 14 (2012) 2216–2228.
- [64] T. Machej, J. Haber, A.M. Turek, I.E. Wachs, *Appl. Catal.* 70 (1991) 115–128.
- [65] G. Tsilomelekis, S. Boghosian, *Catal. Sci. Technol.* 3 (2013) 1869–1888.
- [66] B.M. Weckhuysen, A.A. Verberckmoes, J. Debaere, K. Ooms, I. Langhans, R.A. Schoonheydt, *J. Mol. Catal. A: Chem.* 151 (2000) 115–131.
- [67] A.M. Beale, A.M. van der Eerden, K. Kervinen, M.A. Newton, B.M. Weckhuysen, *Chem. Commun.* (2005) 3015–3017.
- [68] C.M. Mömning, S. Frömel, G. Kehr, R. Fröhlich, S. Grimme, G. Erker, *J. Am. Chem. Soc.* 131 (2009) 12280–12289.
- [69] M.V. Frash, R.A. van Santen, *Phys. Chem. Chem. Phys.* 2 (2000) 1085–1089.
- [70] C.A. Gärtner, A.C. van Veen, J.A. Lercher, *ChemCatChem* 5 (2013) 3196–3217.
- [71] E. Thorsteinson, T. Wilson, F. Young, P. Kasai, *J. Catal.* 52 (1978) 116–132.
- [72] B. Sarkar, R. Goyal, C. Pendem, T. Sasaki, R. Bal, *J. Mol. Catal. A: Chem.* 424 (2016) 17–26.